⌘ *Author's Choice*

THE JOURNAL OF BIOLOGICAL CHEMISTRY VOL. 287, NO. 52, pp. 43753–43764, December 21, 2012
© 2012 by The American Society for Biochemistry and Molecular Biology, Inc. Published in the U.S.A.

Electrostatic Ratchet in the Protective Antigen Channel Promotes Anthrax Toxin Translocation*[S]

Received for publication, September 14, 2012, and in revised form, October 30, 2012 Published, JBC Papers in Press, October 31, 2012, DOI 10.1074/jbc.M112.419598

Sarah L. Wynia-Smith[‡], Michael J. Brown[§], Gina Chirichella[¶], Gigi Kemalyan[‖], and Bryan A. Krantz[‡§¶1]

From the [‡]California Institute for Quantitative Biosciences, the Departments of [§]Molecular & Cell Biology and [¶]Chemistry, and the [‖]Howard Hughes Medical Institute, University of California, Berkeley, California 94720

Background: Ratchets are key features in molecular machines that unfold and transport biopolymers.
Results: An electrostatic ratchet in the anthrax toxin protein translocase was experimentally identified and modeled.
Conclusion: The anthrax toxin translocase harnesses the proton motive force with an electrostatic ratchet.
Significance: This report describes an electrostatic ratchet element critical to proton motive force-driven translocation.

Central to the power-stroke and Brownian-ratchet mechanisms of protein translocation is the process through which nonequilibrium fluctuations are rectified or ratcheted by the molecular motor to transport substrate proteins along a specific axis. We investigated the ratchet mechanism using anthrax toxin as a model. Anthrax toxin is a tripartite toxin comprised of the protective antigen (PA) component, a homooligomeric transmembrane translocase, which translocates two other enzyme components, lethal factor (LF) and edema factor (EF), into the cytosol of the host cell under the proton motive force (PMF). The PA-binding domains of LF and EF (LF_N and EF_N) possess identical folds and similar solution stabilities; however, EF_N translocates ~10–200-fold slower than LF_N, depending on the electrical potential ($\Delta\psi$) and chemical potential (ΔpH) compositions of the PMF. From an analysis of LF_N/EF_N chimera proteins, we identified two 10-residue cassettes comprised of charged sequence that were responsible for the impaired translocation kinetics of EF_N. These cassettes have nonspecific electrostatic requirements: one surprisingly prefers acidic residues when driven by either a $\Delta\psi$ or a ΔpH; the second requires basic residues only when driven by a $\Delta\psi$. Through modeling and experiment, we identified a charged surface in the PA channel responsible for charge selectivity. The charged surface latches the substrate and promotes PMF-driven transport. We propose an electrostatic ratchet in the channel, comprised of opposing rings of charged residues, enforces directionality by interacting with charged cassettes in the substrate, thereby generating forces sufficient to drive unfolding.

Protein translocation is a fundamental molecular process required to transport proteins across membranes and to disassemble, denature, renature, and/or degrade proteins within the cell (1, 2). Many biological events depend upon protein translocation (3), namely microbial toxin translocation into host cells (1, 2, 4–9), toxin secretion (10), antigen presentation (11), membrane and organelle biogenesis (12), and retrograde transport of misprocessed proteins from the endoplasmic reticulum (11). The translocase machinery is generally, but not always (13), comprised of proteinaceous components. Although diverse in mechanism, translocases utilize common driving forces such as ATP hydrolysis or the proton motive force (PMF)[2] to provide the necessary energy for unfolding and translocation (1).

Brownian-ratchet (BR) (Fig. 1*A*) and power-stroke (PS) (Fig. 1*B*) mechanisms have been invoked to describe how molecular machines convert potential energy (the PMF or ATP) into useful work, such as unfolding and translocating proteins (2). The PS mechanism is believed to do work via a direct chemomechanical coupling of the energy source, whereas the BR mechanism does work by rectifying Brownian motion. In each case, the PS and BR mechanisms function via a cyclical dissipation of the potential energy source, creating repeated nonequilibrium fluctuations in the system. The substrate polymer is then directed to move in a unidirectional manner by means of some type of rectification or ratchet mechanism. The ratchet can be thought of energetically as an asymmetrical potential energy barrier that fluctuates as the energy source dissipates, or structurally, as a loop that forcefully pushes the peptide in one direction and/or biases against retro-translocation. The molecular bases of these ratchet features are not well understood.

Anthrax toxin (1, 2, 14), the tripartite virulence factor secreted by *Bacillus anthracis* (the etiologic agent of anthrax), is ideally suited for biophysical studies probing the molecular mechanism of PMF-driven protein translocation (1, 4–9, 15–18) (Fig. 1*C*). Using electrophysiology, the electrical potential ($\Delta\psi$) and chemical potential (ΔpH) compositions of the PMF can be externally controlled (4–9, 16, 17). Lethal factor (LF) and edema factor (EF) are the two different ~90-kDa enzyme components of the toxin, which are translocated by the oligomeric channel formed by a third component, protective antigen (PA, 83 kDa).

* This work was supported, in whole or in part, by National Institutes of Health Grant R01-AI077703 and University of California start-up funds.
⌘ *Author's Choice*—Final version full access.
[S] This article contains supplemental Tables S1–S3 and Figs. S1 and S2.
[1] To whom correspondence should be addressed: 476 Stanley Hall 3220, Berkeley, CA 94720. E-mail: bakrantz@berkeley.edu.

[2] The abbreviations used are: PMF, proton motive force; α clamp, α helix clamp; $\Delta\psi$, membrane potential; $\Delta\psi_{rev}$, reversal potential; $\Delta G^{\ddagger}$, activation energy; ΔG_{NI}, equilibrium stability between native and intermediate states; ΔpH, proton gradient; ϕ clamp, phenylalanine clamp; BR, Brownian ratchet; EF, edema factor; EF_N, EF amino-terminal PA-binding domain; LF, lethal factor; LF_N, LF amino-terminal PA-binding domain; PA, protective antigen; PS, power stroke.

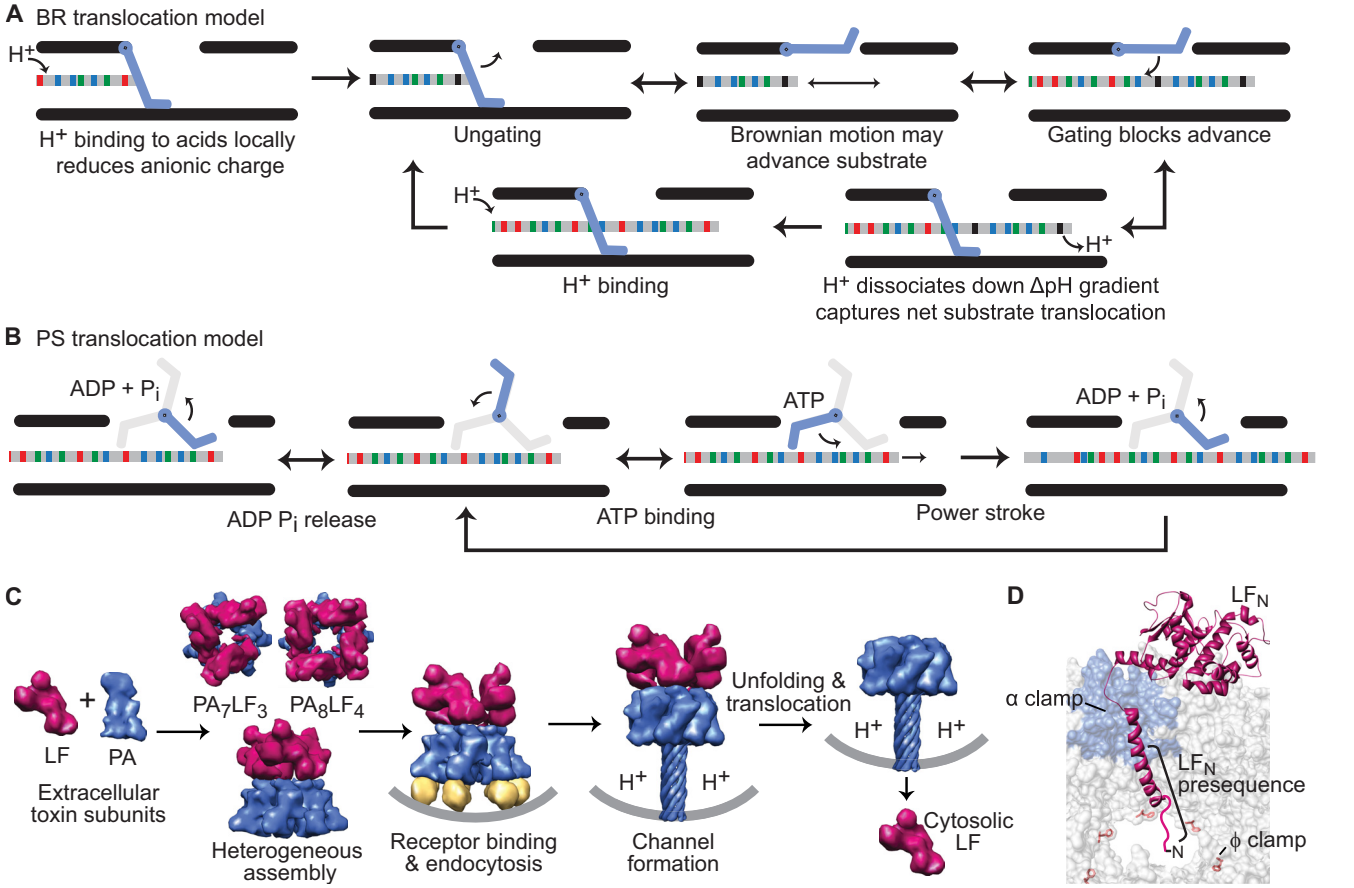

FIGURE 1. **Models of translocation.** Shown are (*A*) H^+-powered BR and (*B*) ATP-driven PS protein-translocation models. The translocating peptide has its residue chemistries colored: deprotonated acidic (*red*), protonated acidic (*black*), basic (*blue*), and hydrophobic (*green*). Dynamic gates and clamps that cycle in these systems are shown as *steel blue*. See text for details. *C*, assembly and translocation mechanism of anthrax lethal toxin. The components of lethal toxin, PA (*steel blue*) (21, 42), and LF (*magenta*) (24), assemble into heterogeneous oligomeric complexes, PA_8LF_4 (4) and PA_7LF_3, which are then endocytosed upon binding a receptor (*gold*). Acidification triggers the PA oligomer to form a translocase channel (19, 23, 43), and the ΔpH component of the PMF drives LF unfolding and translocation into the cytosol (6, 8, 9). *D*, the PA oligomer (*gray surface*) facilitates LF (*magenta*) unfolding and translocation with several known polypeptide clamps. The α clamp (*light blue surface*) (42) binds nonspecifically to peptide helices and initiates LF_N (*magenta*) translocation by binding to its first helix, α1, which is just carboxyl-terminal to the modeled amino-terminal leader sequence leading into the central lumen. The ϕ clamp, a ring of 7 or 8 Phe-427 residues (*red sticks*) in the PA oligomer, which is depicted here in the prechannel conformation to show its approximate location, then engages the amino-terminal leader sequence again through nonspecific interactions (7). These clamps may work in concert to bind and release substrate promoting unfolding and translocation (2).

To function, PA, LF, and EF must assemble into holotoxin complexes (Fig. 1*C*). PA is initially cleaved by a furin-type protease. The resulting 63-kDa PA subunits assemble into either heptameric (PA_7) (19–21) or octameric (PA_8) (4, 5, 22, 23) oligomers, or prechannels. PA_7 and PA_8 can bind up to three and four EF/LF moieties, respectively (4, 5). Crystal structures of LF (24), EF (25, 26), PA (21), the PA_7 (20) and PA_8 (5) prechannel oligomers, and the core of a PA_8LF_4 holotoxin complex (4) have been described. Once assembled, toxin complexes are endocytosed and trafficked to an acidic compartment in the cell, where PA converts to a cation-selective channel (27). The channel structure as resolved by electron microscopy (EM) (19) has a putative extended tubular β-barrel architecture (28, 29), analogous to the *Staphlococcus aureus* α-hemolysin toxin pore (30).

The narrowness of the PA channel requires that LF and EF unfold during translocation. Some destabilization of these proteins is imparted by the acidic conditions of the endosome (31). Interestingly, some unfolding occurs when LF and EF initially form a complex with the PA oligomer. In a recent crystal structure of the core of the PA_8LF_4 holotoxin, it was determined that the first α helix and β strand of the amino-terminal PA-binding domain of LF (LF_N) are unfolded and docked into a cleft, called the α clamp (4) (Fig. 1*D*). The α clamp is created at the interface of adjacent PA subunits, such that the deep cleft is framed by twin Ca^{2+}-ion binding sites (4). The α clamp is also a highly nonspecific binding site, and can interact with diverse sequence chemistries, binding amphipathic and nonamphipathic helices with similar affinities (4). Detailed mutagenesis studies have shown that the most force-dependent step of the translocation mechanism coincides with the unfolding of the remaining structure of LF_N (8). In fact, to cross the rate-limiting barrier, a significant portion of the amino-terminal β-sheet subdomain of LF is required to unfold (8). The unfolding process appears to also require another unfoldase active site, called the ϕ clamp (7, 8). The ϕ clamp is a ring of Phe-427 residues, which also bind nonspecifically to substrates that are dense in aromatic, hydrophobic, and cationic functional groups (7) (Fig. 1*D*). These two unique protein-denaturation sites in the PA channel (α and ϕ clamps) together favor the unfolding process. Although the mechanism is uncertain, these protein-denaturation sites are

not thought to be traditional protein-binding sites; rather they are believed to be dynamic, coordinated, and ratchet-like, switching between high and low affinity states to promote directional motion, where binding at one clamp site can allosterically control binding at the other clamp site (1).

Although translocation can be driven by either the $\Delta\psi$ (15) or ΔpH (6), the ΔpH is sufficient (9) and critical to the efficient translocation of the full-length enzymes, LF and EF (6). A consensus picture is emerging that the underlying mechanism of ΔpH-driven translocation involves a charge-state BR (6, 8, 9, 16–18). Differences in the relative rates of protonation on either side of the membrane are believed to be able to bias Brownian fluctuations and impart directionality in the translocation mechanism. Brown *et al.* (9) have shown that acidic residues in a protein substrate are required for ΔpH-driven translocation. These residues are effectively the molecular teeth upon which an electrostatic ratchet feature within the channel acts to produce forces during translocation.

An anionic charge requirement for ΔpH-dependent protein translocation may seem unusual, as the PA channel itself is strongly cation selective (or anion repulsive) (27). However, the protonation of acidic residues is likely required to make a portion of the translocating chain within the channel near neutral or slightly cationic. Doing so allows the protein to pass through the anion-rejection site of the channel by means of Brownian motion (Fig. 1*A*). Once the protonated portion of the translocating protein reaches the higher pH of the cytosol, these sites are more frequently deprotonated, becoming electrostatically incompatible with the channel. The same electrostatic feature that repels anion flux into the channel may then also act to ratchet and exclude retrograde efflux back into the channel. This rectification/ratchet feature is a critical aspect of BR- and PS-type molecular machines, because it can bias nonequilibrium substrate fluctuations by limiting retrograde efflux.

Cycles of substrate protonation, Brownian motion, and deprotonation are likely required to pull the protein across the membrane. Analogously, with ATP-dependent systems, 100s of cycles of ATP binding and hydrolysis are required to unfold and transport a substrate protein. Several critical questions remain unanswered as to how this mechanism applies to protein translocation. What substrate sequence features allow for rapid translocation? What feature in the channel rectifies or ratchets Brownian motion and nonequilibrium fluctuations? How does the proposed charge-state BR mechanism develop forces sufficient to unfold substrate proteins? To address these questions, we investigated electrostatic requirements of the substrate and channel in PMF-driven anthrax toxin translocation. Our results and modeling studies are consistent with an electrostatic ratchet translocation model.

EXPERIMENTAL PROCEDURES

Proteins—Recombinant wild-type (WT) PA, LF_N, the amino-terminal PA-binding domain of EF (EF_N), and resulting chimeras and mutants were expressed and purified as described (5, 8). Assembly PCR was used to construct LF_N/EF_N chimeras (4, 9). The amino-terminal six-histidine affinity tags (His_6) were removed from LF_N/EF_N chimeras using bovine α thrombin (8). PA_7 prechannel oligomers were assembled as described (5). For the PA mutants PA_{top} (containing the substitutions D276S, D335S, and E343S) and PA_{bot} (containing the substitutions E302T, H304T, E308T, and H310T), and a WT PA control, 10 μg of each PA monomer was proteolyzed by 0.4 units of furin (New England Biolabs) in 20 mM Tris-Cl, pH 9, 150 mM NaCl, and 1 mM $CaCl_2$ at room temperature. After 30 min, LF_N was added at a 1:1 molar ratio, and following another 30-min incubation at 25 °C, Fos-choline-14 was introduced to a final concentration of 2 mM to stabilize the PA oligomers in the channel form (32). Proper PA assembly was verified by native PAGE, SDS-PAGE, and negative stain EM.

Electrophysiology—Planar lipid bilayers were formed by painting (33) a membrane-forming solution (3% 1,2-diphytanoyl-*sn*-glycerol-3-phosphocholine in *n*-decane) across a 100-μm aperture in a 1-ml white Delrin or polysulfone cup (4, 5, 8). A capacitance test confirmed the quality of the membrane. The membrane separates the *cis* and *trans* chambers, each containing 1 ml of universal bilayer buffer (100 mM KCl, 1 mM EDTA, 10 mM oxalic acid, 10 mM MES, 10 mM phosphoric acid). Ag/AgCl electrodes bathed in saturated 3 M KCl were linked to the chambers via 3 M KCl-agar salt bridges. PA currents were recorded with an Axoclamp 200B amplifier in CLAMPEX10.

Translocation Assays—Bilayers were bathed in symmetrical universal bilayer buffer. PA_7 prechannels were added to the *cis* chamber (held at 20 mV), and conductance was blocked by the addition of substrate (LF_N, EF_N, or chimera) to the *cis* side (held at 20 mV in symmetric pH 5.6 experiments). The substrate blockade was >95% of the original current. Excess substrate was perfused by a hand-cranked, push-pull perfusion system. In $\Delta\psi$-driven translocation assays, substrate translocation was initiated by increasing the $\Delta\psi$; $\Delta\psi \equiv \psi_{cis} - \psi_{trans}$ ($\psi_{trans} \equiv 0$). Translocation activation energy ($\Delta G^{\ddagger}$) was computed by $RT \ln t_{1/2}/c$ (8). The $t_{1/2}$ value is the time for half the substrate to translocate; c is a 1-s reference; R is the gas constant; and T is the temperature. In ΔpH-driven experiments, the *cis* and *trans* chambers were bathed in universal bilayer buffer differing only in pH (pH_{cis} = 5.6; pH_{trans} = 6.6), where $\Delta pH \equiv pH_{trans} - pH_{cis}$. The $\Delta\psi$ was −1 mV during substrate blockade and perfusion. Translocation was initiated by increasing $\Delta\psi$ to 20 mV. Translocation records in either case were acquired across a range of $\Delta\psi$ values (n = 6 to 30).

Equilibrium Stability Measurements—Guanidinium chloride titrations of LF_N, EF_N, and chimeras were carried out as described (1, 2) in 10 mM sodium phosphate, 1 M glucose, pH 7.5, at 20 °C. The stabilizing glucose additive was used to define the native state baseline. Each titration point was monitored after reaching equilibrium by circular dichroism (CD) spectroscopy at 222 (±2) nm using a Jasco J-810 spectropolarimeter. The CD-probed curves fit to a four-state thermodynamic model ($N \leftrightarrow I \leftrightarrow J \leftrightarrow U$), where native ($N$), two intermediates ($I$ and J), and an unfolded (U) state are populated (2). We used the thermodynamic difference between the N and I states (ΔG_{NI}) to assess the stability of the protein.

Reversal Potential ($\Delta\psi_{rev}$) Measurements—A planar bilayer was formed with the *cis* chamber bathed in 5 mM potassium phosphate, 100 mM KCl, pH 6.6, and the *trans* chamber bathed in unbuffered saline consisting of 100 mM KCl, pH 5.8. Assembled mutant and WT PA oligomer-LF_N prechannel complexes

were added to the *cis* side. Following channel insertion, the *cis* chamber was perfused thoroughly with fresh 100 mM KCl, making the system symmetrical, unbuffered KCl, pH 5.8. Residual LF_N was then removed by applying a strong 100 mV $\Delta\psi$ to translocate it through the channel; and in some cases, a 1-unit ΔpH was established to aid in channel clearance of residual LF_N. Upon stabilization, a series of 50-μl aliquots of 3 M KCl were added to the *cis* side, and $\Delta\psi_{rev}$ was recorded as the $\Delta\psi$ required to drop the current to zero. All given KCl ratios of the two sides of the bilayer have been corrected for activity in water (34), and following the experiment, the chambers were weighed to confirm their volume.

Ensemble Channel Blocking—A planar bilayer was formed with both chambers in 10 mM potassium phosphate, pH 6.6. The *cis* chamber alone had an additional 100 mM equivalent of KCl. Assembled mutant and WT PA oligomer-LF_N prechannel complexes were added to the *cis* side, and the chamber was perfused following insertion. To remove remaining LF_N, 10 μl of 0.4 M phosphoric acid was added to the *cis* chamber to lower the pH to ~4.4, and a $\Delta\psi$ of 20 mV was applied. Afterward, the *cis* chamber was perfused with fresh pH 6.6 buffer, and the $\Delta\psi$ was returned to 0 mV. LF_N was added to a given concentration and allowed equilibrate. The percent blockade was determined by the equilibrium drop in current following the addition of LF_N.

EM—Preparations of PA_{top}, PA_{bot}, and a WT PA control were purified by anion exchange chromatography to remove residual PA monomer and excess LF_N. Fos-choline-14 was only added to a concentration of 0.05 mM to avoid reaching the critical micelle concentration. All samples were diluted to an estimated final concentration of 70 nM (based on absorbance at 280 nm). Diluted complexes were incubated for 30 s on 400-mesh copper grids (Electron Microscopy Sciences) coated with continuous carbon on nitrocellulose, stained with 1% uranyl formate, and imaged with a Tecnai 12 TEM operated at 120 kV and at ×49,000 magnification. Single particles were selected automatically using boxer (EMAN). The total numbers of particles (n) analyzed were: PA WT (n = 4847), PA_{top} (n = 4577), and PA_{bot} (n = 4971). Class averages were determined iteratively using 10 successive cycles of Adapt, an automated classification program (written in house) and two-dimensional multireference alignment in IMAGIC.

Molecular Models—EF_N and LF_N domains from EF (PDB 1Y0V (26)) and LF (PDB 1J7N (24)), respectively, were α-carbon-(C_α)-aligned in CHIMERA (35). A three-dimensional model of the 14-stranded β-barrel region of the PA channel (residues 275 to 352) was made by coaxially stacking multiple copies of the heptameric β-barrel from α hemolysin (PDB 7AHL (30)). Peptide bonds were formed and residues were repopulated using COOT (36). The model was aligned to the z axis in CHIMERA (35). To obtain an electrostatic energy $U(z)$ as a function of the distance moved axially through the barrel z axis, we computed the sum of all pairwise electrostatic energies in a PERL script (zforce.pl, which is available on request), using a 1-unit elementary point charge, q_{test}, moved along the center of the barrel in 0.1-Å increments, $U(z) = q_{test}\, b \sum q_i \cos\theta_i/d_i$, where d_i is the distance between the C_α of the ith charged site within the channel of elementary charge, q_i, and q_{test}; θ_i is the angle between the charges and the z axis; and b is an electrostatic energy conversion constant of 1390 kJ Å mol^{-1}.

RESULTS

EF_N Translocates Slower Than LF_N—LF_N and EF_N share high levels of sequence (37) and structural homology (24, 26); however, the most divergent sequence homology occurs on the amino terminus (Fig. 2*A*). In planar lipid bilayer electrophysiology experiments, LF_N and EF_N translocate through the PA channel at remarkably different rates. Although LF_N translocates with a $t_{½}$ value of ~10 s at symmetrical pH 5.6 and a $\Delta\psi$ of 60 mV (6, 8), His_6-EF_N translocates with a $t_{½}$ of ~140 s under identical conditions (5). The His_6 tag used in affinity purification tends to have modest effects on the translocation $t_{½}$ (9), and so we re-examined these translocation differences under two different driving force extremes, a pure $\Delta\psi$ and a strong ΔpH, using the constructs in which the His_6 tag was removed by a protease. In our electrophysiological assay (6–8), a planar lipid bilayer separates two aqueous chambers (*cis* and *trans*). We first insert PA_7 channels into the bilayer. Either WT LF_N or EF_N was added to the *cis* side of the membrane (side to which PA_7 was added). Generally, an exponential decrease in current is observed as the amino-terminal presequence of the substrate inserts into the ion-conducting PA channel (38). A brief perfusion removes excess substrate from the *cis* chamber, and translocation is initiated by changing the $\Delta\psi$ and/or ΔpH. The subsequent current increase results from substrate translocation to the *trans* side of the membrane, as determined by control experiments (6, 15). Two parameters are obtained from these "single turnover" translocation records: the $t_{½}$ and the efficiency of translocation, which is equivalent to the fraction of substrate that successfully translocates. We note that there are multiple LF_N or EF_N bound to each PA complex so these translocation records likely represent the turnover of several substrates. Therefore, single turnover kinetics refers to a single loaded PA complex that has translocated all of its substrates. We analyzed LF_N and EF_N translocation under identical conditions. Under a pure $\Delta\psi$ driving force, EF_N translocated ~200-fold slower than LF_N (Fig. 2*B*). Likewise, under a 1-unit ΔpH, EF_N translocated ~10-fold slower than LF_N (Fig. 2*C*). Interestingly, previous studies (31) and our more recent thermodynamic analysis (Fig. 2*D* and supplemental Table S1) show that the equilibrium stability of EF_N, ΔG_{NI}, is ~2.4 kcal mol^{-1} less stable than LF_N (31). As destabilization should in the most extreme case increase the rate of translocation due to the lowered unfolding barrier (8), it is unlikely that the weakened solution thermodynamic stability of EF_N explains the observed increase in the activation energy of translocation relative to LF_N.

Amino-terminal Chimeras with LF_N Complement Slow EF_N Translocation—To determine the sequence differences responsible for the relatively slow translocation of EF_N, we created a series of chimera constructs (Fig. 2*A*). In these, we used the bulk of the EF_N domain and only replaced the amino-terminal peptide with the corresponding sequence from LF_N, where specifically 10, 18, 22, 26, 30, 40, or 50 LF_N residues replaced equivalent positions in the EF_N construct. (In our scheme, $LF_{1\text{-}a}EF_{b\text{-}254}$, a and b inclusively delimit the last residue

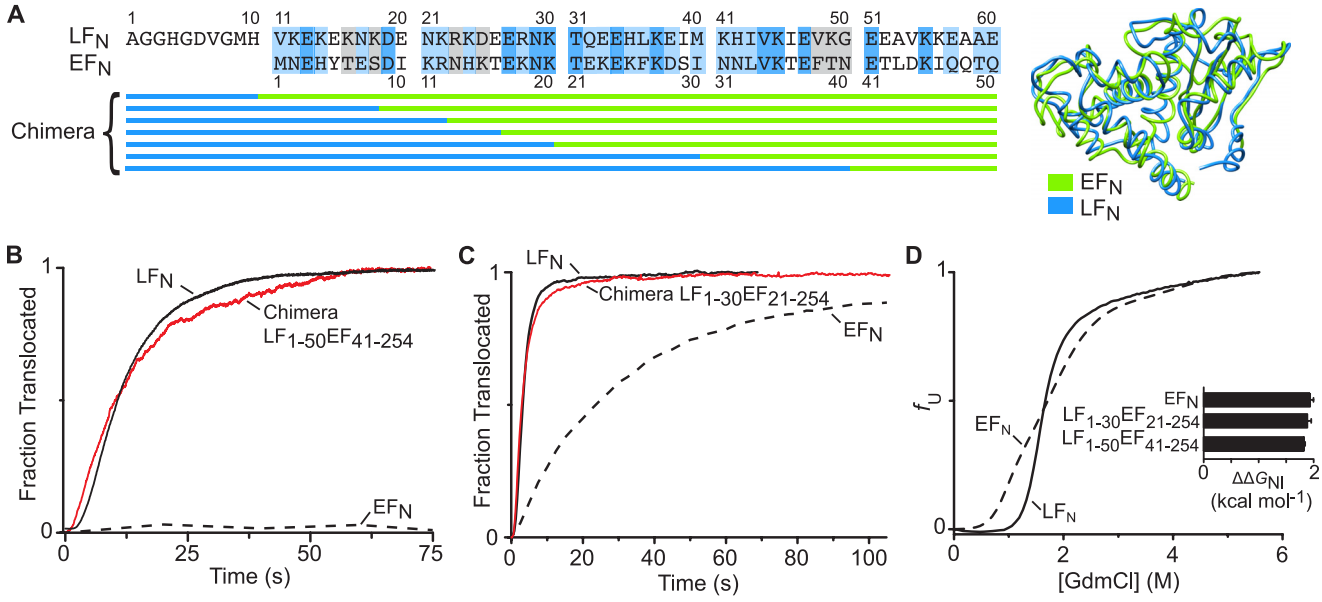

FIGURE 2. **LF_N/EF_N chimeras are sufficient to mimic LF_N-like translocation kinetics.** *A* (*left*), sequence alignment of the first 50 amino acids of LF_N and EF_N. Residue pairs are shaded as follows: identity (*blue*), similarity (*light blue*), and weak similarity (*gray*). LF_N/EF_N chimera constructs are shown below where the increasing amounts of amino-terminal sequence from LF_N (*blue*) appended to the EF_N carboxyl-terminal folded domain (*green*). *Right*, C_α-backbone alignment of EF_N (1Y0V, *green*) and LF_N (1J7N, *blue*) computed in CHIMERA (35). *B*, representative translocation recordings of LF_N (*black*), EF_N (*dashed*), and $LF_{1-50}EF_{41-254}$ (*red*) under a $\Delta\psi$ driving force (at symmetric pH 5.6, $\Delta\psi$ of 50 mV). *C*, representative translocation records of LF_N (*black*), EF_N (*dashed*), and $LF_{1-30}EF_{21-254}$ (*red*) under a 1-unit ΔpH driving force (5.6 pH_{cis}, 6.6 pH_{trans}, $\Delta\psi$ of 20 mV). Records in *panels B* and *C* are normalized to maximal expected fraction translocated. *D*, representative equilibrium denaturant titrations comparing LF_N (*solid*) and EF_N (*dashed*) in guanidinium chloride (1 M glucose, pH 7.5, 20 °C) probed by CD at 222 nm and normalized to fraction unfolded (f_U). *Inset*, equilibrium stability differences ($\Delta\Delta G_{NI}$) are referenced to WT LF_N (where $\Delta\Delta G_{NI}$ compares EF_N and chimeras to LF_N). For other chimeras, see supplemental Table S1. Error are the mean ± S.D. for $n = 3$.

of LF_N and starting residue of EF_N, respectively.) We found that the $LF_{1-50}EF_{41-254}$ and $LF_{1-30}EF_{21-254}$ chimeras represented the minimal chimera constructs (Fig. 2, *B* and *C*) of all tested chimeras (supplemental Fig. S1, *A* and *B*) to exhibit LF_N-like translocation under a pure $\Delta\psi$ and a 1-unit ΔpH, respectively. The sequence determinants that define the relatively slow translocation kinetics of EF_N are found on its amino terminus. Thus the translocation kinetic stabilization we observe with EF_N relative to LF_N cannot be attributed to a phenomenon that occurs in solution (in isolation), but rather this difference manifests only in the context of the unfolding machine, the PA channel (Fig. 2*D*).

We then further explored the translocation differences of these chimeras under a variety of driving force conditions. Under pure $\Delta\psi$-driven translocation at symmetric pH, we found that the more LF_N sequence introduced into the chimera, the faster the rate of translocation (supplemental Fig. S1*A*). Due to the complex nature of these ensemble translocation kinetics, a rate constant for translocation, k, was estimated using the $t_{1/2}$ for translocation, as $k \propto 1/t_{1/2}$, and from this we compute the $\Delta G^{\ddagger}$. Interestingly, we found the $LF_{1-10}EF_{1-254}$ chimera had similar to slightly slower translocation rates than EF_N across many $\Delta\psi$ values (supplemental Fig. S1*C*), indicating that these additional 10 residues in LF_N are not responsible for the observed differences in translocation. To effectively recapitulate the LF_N $\Delta\psi$-dependence curve, the $LF_{1-50}EF_{41-254}$ chimera was sufficient.

We then examined the set of chimeras under a 1-unit ΔpH gradient (supplemental Fig. S1*B*). Interestingly, the $LF_{1-10}EF_{1-254}$ and $LF_{1-18}EF_{9-254}$ chimeras showed slower translocation than EF_N (supplemental Fig. S1*D*), indicating potentially that these sequences, which have more densely hydrophobic amino termini (Fig. 2*A*), may impede translocation due to the formation of an unusually tight binding interaction at the ϕ-clamp site. We found that the $LF_{1-30}EF_{21-254}$ chimera, however, was sufficient to completely restore LF_N-like translocation (Fig. 2*C* and supplemental Fig. S1*D*); and in contrast to purely $\Delta\psi$ driving forces, the sequence determinant for this restoration was concentrated between LF_N residues 20 and 30.

Two Sequence Cassettes Modulate the Translocation Stability of EF_N and LF_N—A summary of the $\Delta\psi$- and ΔpH-driven translocation results (Fig. 3*A*) identified two sequence regions of interest, or "cassettes:" (i) the 20s cassette (residues 19–30); and (ii) the 40s cassette (residues 41–50) (Fig. 3*B*). (Note that because EF_N is 10 residues shorter than LF_N on the amino-terminal end, we are applying the LF_N-numbering scheme to EF_N.) Under symmetric pH conditions and a $\Delta\psi$ driving force, there is a ~1.3 kcal mol^{-1} difference in $\Delta G^{\ddagger}$ between $LF_{1-18}EF_{9-254}$ and $LF_{1-26}EF_{17-254}$ in the 20s cassette (Fig. 3*A*). Under a 1-unit ΔpH gradient, there is a ~2 kcal mol^{-1} difference between the same chimeras (Fig. 3*A*). Also notable is the ~1.5 kcal mol^{-1} $\Delta G^{\ddagger}$ difference between the $LF_{1-40}EF_{31-254}$ and $LF_{1-50}EF_{41-254}$ chimeras (Fig. 3*A*); however, this difference was only observed under a $\Delta\psi$ driving force. Therefore, we hypothesize that sequence divergences in the 20s and 40s cassettes are responsible for the slow translocation kinetics of EF_N.

Mutations in these two sequence cassettes may have destabilized the chimera and altered the unfolding step of the translocation mechanism. To test this possibility, we measured ΔG_{NI} of the base and most highly internally mutagenized chimera constructs using standard solution unfolding procedures (8, 31). We generally found no significant differences in ΔG_{NI}

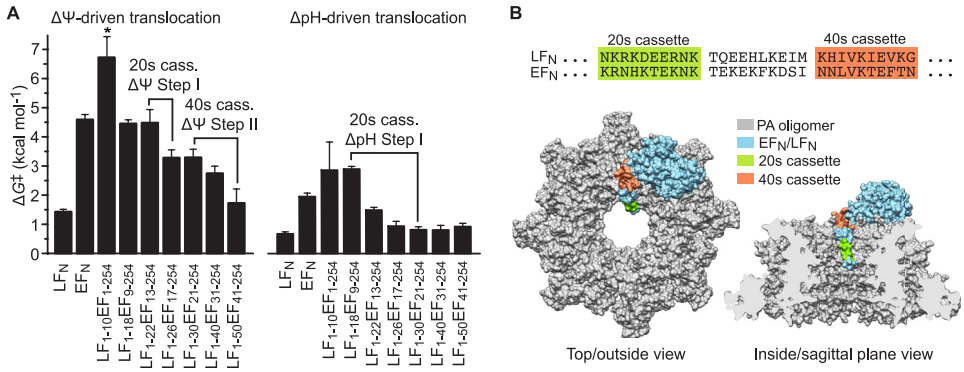

FIGURE 3. **Charged residues in the 20s and 40s cassettes utilize the Δψ and ΔpH driving forces to promote unfolding and translocation.** *A* (*left*), translocation activation energy for chimeric constructs at symmetric pH 5.6 and Δψ of 50 mV. One value was estimated by extrapolation (*) based on a larger Δψ-dependent dataset (supplemental Fig. S1*C*) and associated fit parameters (supplemental Table S2). *Right*, translocation $\Delta G^{\ddagger}$ for LF_N, EF_N, and the indicated LF_N/EF_N chimeras under a 1-unit ΔpH (5.6 pH_{cis}, 6.6 pH_{trans}, Δψ of 20 mV). *Brackets* indicate significant differences (or "steps") in $\Delta G^{\ddagger}$ due to inclusion of the intervening LF_N sequence cassette (*cass.*) Additional Δψ-dependent data at a 1-unit ΔpH are given in supplemental Fig. S1*D*, where associated fit parameters are given in supplemental Table S3. *B* (*above*), amino-terminal 20s (*green*) and 40s (*orange*) cassette peptides are highlighted and the residue sequences in LF_N and EF_N are shown. *Below*, *top/outside* and *inside/sagittal plane* vantages of a molecular model of LF_N (*blue*) in complex with the PA_8 oligomer (*gray*) (PDB 3KWV (4)).

between these chimeras and EF_N (Fig. 2*D* and supplemental Table S1). As the bulk of the folded domain is from EF_N, this result was expected. The residues differing between the chimeras are contained in the amino-terminal unstructured region and first α helix and β strand, which are highly solvent accessible. Thus we ruled out protein destabilization for these chimeras, and the amino-terminal sequence divergence in EF_N likely affects the mechanisms of PA channel-dependent unfolding and translocation.

Charge Content of Cassettes Controls Driving Force Dependence of Translocation—To identify sequence features in the two cassettes contributing to the observed translocation $\Delta G^{\ddagger}$ differences, we introduced several point mutations within the existing chimera constructs (Fig. 4, *A* and *B*). These mutations were made given the variation in net charge (z) observed within the cassettes. Net charge was estimated by $z = n_{basic} - n_{acidic}$, where n_{basic} and n_{acidic} are the number of basic and acidic residues, respectively. For the 20s cassette, we found that EF_N and LF_N had fairly different z values of +5 and 0, respectively. Likewise, for the 40s cassette, EF_N and LF_N had z values of 0 and +3, respectively. Upon our examination of their translocation kinetics, we found that correlations emerged between z values within the cassettes and their translocation $\Delta G^{\ddagger}$ values (Fig. 4, *C* and *D*). Thus as expected, the subtraction of positive charge in the 20s cassette and addition of positive charge in the 40s cassette tended to generally increase the rate of translocation for EF_N-based chimeras.

We also examined the residue identity and position dependence of these effects. When we separately introduced an Asp at positions 23 and 28 of $LF_{1-22}EF_{13-254}$ ($LF_{1-22}EF_{13-254}$ N23D, $z = +1$; $LF_{1-22}EF_{13-254}$ K28D, $z = 0$) (Fig. 4*A*), the rate of translocation increased relative to the parent construct ($z = +2$) (Fig. 4*C*). Furthermore, both $LF_{1-22}EF_{13-254}$ K25D and $LF_{1-22}EF_{13-254}$ K25E ($z = 0$) increased the translocation rate similarly, indicating that there is a general requirement for negative charge, but residue identity is not critical. In general when examining all the data, translocation rates were only affected by changes in z values and not by changes in the position of the charges (Fig. 4*C*). The rate of translocation is similar for the $LF_{1-22}EF_{13-254}$ K25D/T26E and $LF_{1-22}EF_{13-254}$ H24D/K25N chimeras ($z = -1$). Finally, the negative charge neutralizing mutation $LF_{1-25}EF_{16-254}$ D25N ($z = +2$) showed slowed translocation compared with its parent construct $LF_{1-25}EF_{16-254}$ ($z = +1$). A similar but opposite effect can be seen in the 40s cassette, where there is a general requirement for positive charges independent of the specific positions (Fig. 4*D*). For example, $LF_{1-40}EF_{31-254}$ N41E and $LF_{1-40}EF_{31-254}$ T49E ($z = -1$) had similarly decreased translocation rates relative to their parent chimera ($z = 0$). Thus we conclude that the 20s and 40s cassettes indeed have particular anionic and cationic charge requirements, respectively, but these requirements are highly nonspecific in terms of both position and residue identity.

Although most of the charge-dependent $\Delta G^{\ddagger}$ data for the 20s cassette is linear with respect to charge, the presence of outlier data at higher negative charge density led to the hypothesis that there may be two barriers in the charge-dependent transport mechanism. Increasing negative charge can lower one barrier; however, the second barrier is either charge insensitive or somewhat inversely dependent on negative charge. To allow for partial-charge character (δ) during each respective barrier crossing (39), we used the following model,

$$\Delta G^{\ddagger}(z) = RT \ln[\exp((\Delta G^{\ddagger\circ}{}_1 + \delta_1 zF\Delta\psi)/RT) + \exp((\Delta G^{\ddagger\circ}{}_2 + \delta_2 zF\Delta\psi)/RT)] \quad \text{(Eq. 1)}$$

where F is Faraday's constant. For the ΔpH-dependent data ($n = 21$), the fit to Equation 1 was significant ($p < 0.001$) (Fig. 4*C*). The δ parameter was obtained for each barrier as $\delta_1 = -0.7$ (±0.4) and $\delta_2 = 1.0$ (±0.2). The corresponding activation energies, $\Delta G^{\ddagger\circ}{}_1$ and $\Delta G^{\ddagger\circ}{}_2$, in the absence of net charge were 0.3 (±0.5) and 0.9 (±0.3), respectively. For the Δψ-dependent translocation ($n = 21$), the fit was also significant ($p < 0.001$) with $\delta_1 = -0.3$ (±0.2) and $\delta_2 = 0.3$ (±0.1) and $\Delta G^{\ddagger\circ}{}_1 = 3.2$ (±0.5) and $\Delta G^{\ddagger\circ}{}_2 = 3.2$ (±0.5) (Fig. 4*C*). Typically, δ values are challenging to interpret: residues may be partially charged due to pK_a shifts; metal ions may bind to the translocating peptide and alter net charge; and finally, only part of the charged region in the substrate may be required to cross the rate-limiting bar-

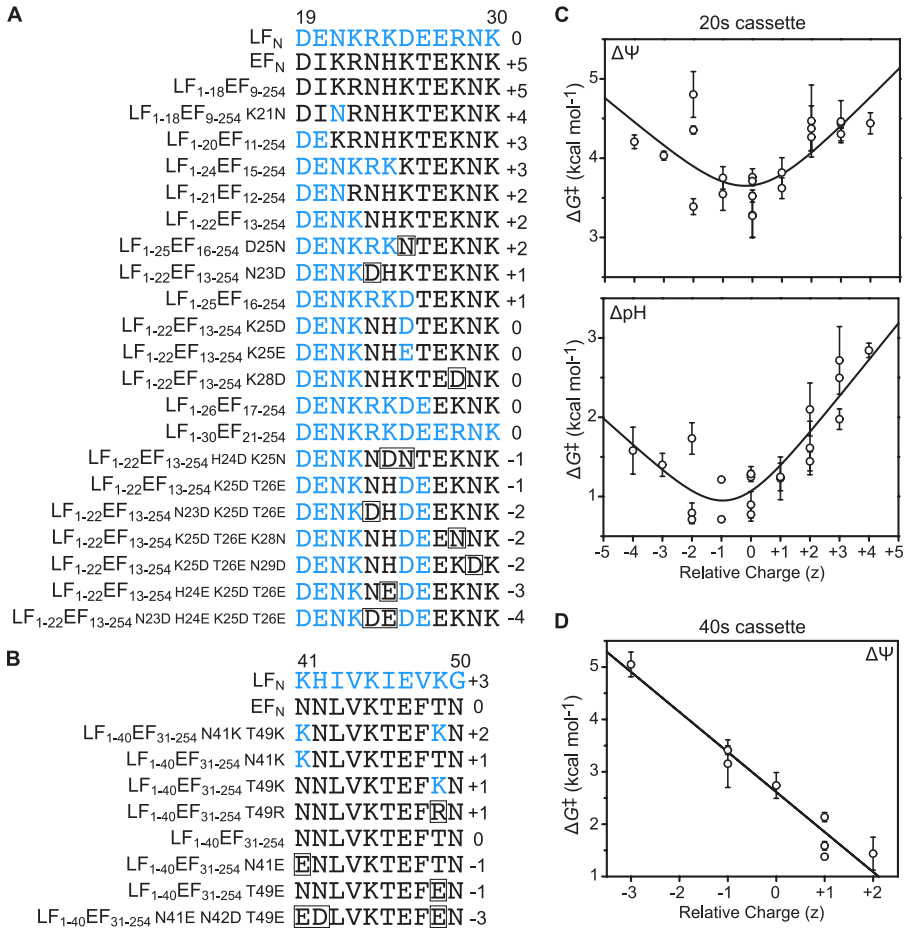

FIGURE 4. **Charged cassettes are nonspecific.** *A*, construct design for chimeras and derivative mutants in the 20s cassette (residues 19–30) are arranged from the most positive to the most negative. Net charge given to the right of each sequence is computed using the following scoring system: *D*, *E* = −1; *H*, *K*, *r* = +1. Residues from native LF_N (*blue*) and native EF_N (*black*) are shown alongside non-native mutations (*boxed*) to either LF_N or EF_N. Residue-numbering scheme is according to LF_N (24). *B*, constructs altering the 40s cassette (residues 41–50). Net charge is computed as in *panel A*. *C* (*top*), $\Delta G^{\ddagger}$ *versus z* at symmetric pH 5.6, $\Delta\psi$ of 50 mV for LF_N/EF_N chimeras and related mutants affecting the 20s cassette (residues 19–30 inclusive). Two-barrier model fit (Equation 1): $\Delta G^{\ddagger o}{}_1 = 3.2$ (±0.5), $\delta_1 = -0.3$ (±0.2), $\Delta G^{\ddagger o}{}_2 = 3.2$ (±0.5), and $\delta_2 = 0.3$ (±0.1) ($n = 21$, $p < 0.001$). *Bottom*, $\Delta G^{\ddagger}$ *versus z* at a $\Delta\psi$ of 20 mV, 1-unit ΔpH (5.6 pH_{cis}, 6.6 pH_{trans}) for the same 20s-cassette variants. Two-barrier fit parameters: $\Delta G^{\ddagger o}{}_1 = 0.3$ (±0.5), $\delta_1 = -0.7$ (±0.4), $\Delta G^{\ddagger o}{}_2 = 0.9$ (±0.3), and $\delta_2 = 1$ (±0.2) ($n = 21$, $p < 0.001$). *D*, $\Delta G^{\ddagger}$ *versus z* at symmetric pH 5.6, $\Delta\psi$ of 50 mV for LF_N/EF_N chimeras and related mutants affecting the 40s-cassette region (residues 41–50 inclusive). Single-barrier model (Equation 2) fit parameters: $\Delta G^{\ddagger o} = 2.7$ (±0.1) and $\delta = -0.58$ (±0.07) ($n = 8$, $p < 0.001$). *Error bars* are the mean ± S.D. ($n \geq 3$).

rier. Nevertheless, the goodness of fit suggests that indeed two unique charge-dependent barriers with inverse charge requirements are present in the translocation mechanism.

In the 40s cassette region (Fig. 4*B*), LF_N possesses additional positive charge comparative to EF_N at positions 41, 42, and 49. We created several point mutations in the existing chimeras to determine the effects of increasing or decreasing charge of the 40s cassette and investigated the charge-based differences in this region via translocation assays (Fig. 4*D*). Starting with a sequence similar to EF_N and increasing its positive charge to that of LF_N, we again observe a direct relationship between charge and the translocation $\Delta G^{\ddagger}$, where increasing positive charge leads to faster translocation. Also the charge dependence was again nonspecific (Fig. 4*D*) where the position and identity of the residues did not appear to matter as much as the overall *z* value (Fig. 4*B*). These charge-dependent data ($n = 8$) for the 40s cassette were best fit by a single-barrier model (39).

$$\Delta G^{\ddagger}(z) = \Delta G^{\ddagger o} + \delta z F \Delta\psi \qquad \text{(Eq. 2)}$$

The fit was significant ($p < 0.001$) with a δ of −0.58 (±0.07) and $\Delta G^{\ddagger o}$ of 2.7 (±0.1) (Fig. 4*D*). The type of cationic-charge preference in the 40s cassette is classical in the sense that it coincides with the direction of the electric field created by the applied membrane potential (*i.e.* the field is *cis*-positive).

Electrostatic Analysis of the PA β Barrel—Given the unusual preference for anionic residues in the 20s cassette when driven by a $\Delta\psi$ (which is exactly opposite of the result expected for a *cis*-positive membrane potential), we hypothesized that the local electrostatic field produced by features within the channel, E_{chan}, may override the electrical potential applied across the membrane, E_m. The overall electric field, *E*, is a vector, where $E = E_{chan} + E_m$. The force applied upon the translocating chain is related to the sign and magnitude of the charge, *q*, of groups in the translocating chain and *E* by $E \times q$. Because the electrical field contributed by the membrane potential relates to $\Delta\psi$ as $E_m = \Delta\psi/d$, where *d* is the distance over which the potential drops, we can assume that the membrane potential will contribute unproductively to a negatively charged sub-

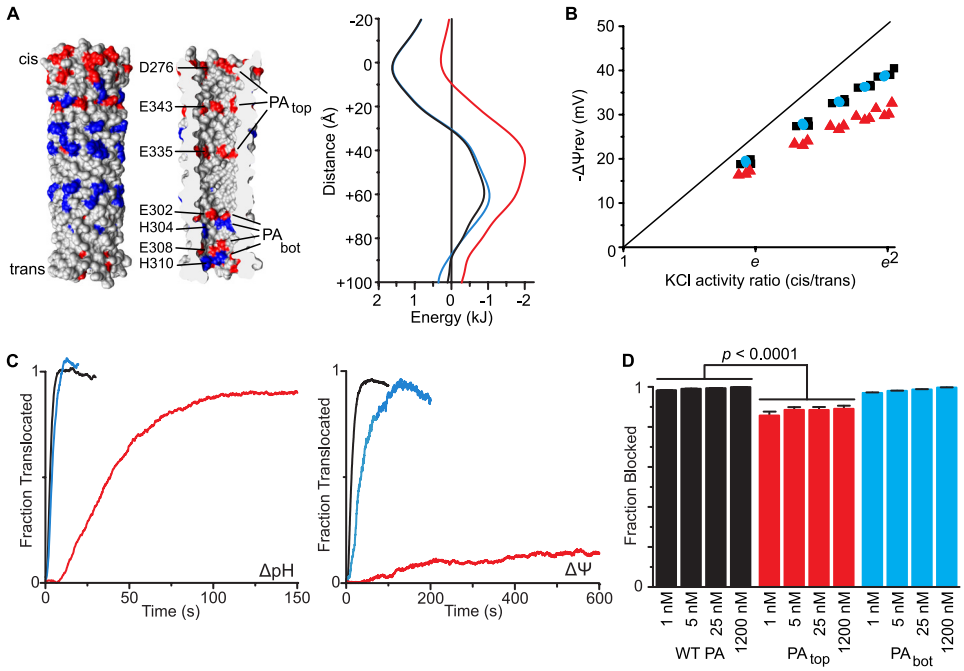

FIGURE 5. **Charge-selectivity filter in PA β barrel is required for efficient translocation.** *A* (*left*), molecular model of the PA channel β barrel (*gray*), where acidic (*red*) and basic (*blue*) residues are highlighted. The outside and a sagittal section of the inside of the β-barrel structure are depicted. *Right,* the electrostatic energy for a negative point charge moved down the central axis of the β barrel of the channel. The origin on the distance axis is at the *cis*-most end of the β barrel, and increasing positive values indicates productive translocation. The potential was computed as described under "Experimental Procedures." *B,* relative differences in ion selectivity for WT PA (*black squares*), PA_{top} (*red triangles*), and PA_{bot} (*blue circles*) determined by $-\Delta\psi_{rev}$ *versus* the KCl activity ratio (*cis*:*trans*). The *x* axis is plotted as a natural log scale marked by factors of *e*. The ideal cation-selective Nernstian relationship (*e*-fold activity ratio per 25.2 mV at 20 °C) is indicated with a *solid line*. Three independent measurements assessed on three different membranes were corrected for membrane and electronics offsets. *C*, representative protein translocation records for WT LF_N under ΔpH (*left*) and $\Delta\psi$ (*right*) using WT PA (*black*), PA_{top} (*red*), and PA_{bot} (*blue*). The $\Delta\psi$ and ΔpH conditions are identical to those applied in Fig. 2, *B* and *C*. Results shown are consistent with replicates obtained on at least two separate membranes. *D*, ensemble bilayer recordings of WT PA (*black*), PA_{top} (*red*), and PA_{bot} (*blue*) channel conductance block by WT LF_N at 1, 5, 25, and 1200 nM were obtained at symmetrical pH 6.6 and no $\Delta\psi$. *Error bars* are the mean ± S.D. ($n = 2$). WT and PA_{top} were tested for significance using an unpaired *t* test ($p < 0.0001$) for all observations ($n = 16$) at each set of conditions.

strate if the membrane potential is positive in polarity. Therefore, E_{chan} likely provides an oppositely oriented electrical field component that can apply a productive force on the substrate that aligns with the productive direction of translocation. Our hypothesis is also supported by the fact that the anion-charge preference in the 20s cassette appears independent of the makeup of the driving force; both $\Delta\psi$-driven and ΔpH-driven kinetics can be accelerated by including additional negative charge in the 20s cassette of EF_N.

To characterize the electrostatic features within the PA channel, we initially built a model of the β barrel portion of the PA channel using the coordinates of α hemolysin (30) (Fig. 5*A*). From this β barrel model, we calculated the sum of all pairwise electrostatic potentials for a point charge translocated along the central axis of the channel ("Experimental Procedures"). Our analysis revealed two prominent and oppositely charged electrostatic features, which were juxtaposed in the β barrel. One is a strongly anion-repulsive feature (PA residue ranges 275–283 and 343–352, generally localized to the top of the β barrel), and the other is a strongly cation-repulsive feature (PA residue ranges 287–299 and 328–340, generally localized to the middle of the β barrel) (Fig. 5*A*). The PA residues contributing to these two features were located both inside and outside of the β barrel. Based on the same analytical model, we produced two β barrel mutants, one that would disrupt the anionic feature and one that would not. PA_{top} disrupted the upper, *cis*-most portion of the β barrel, targeting its negatively charged residues by substituting them with isosteric Ser residues (D276S, D335S, and E343S). We chose Ser or Thr substitutions because the inside of the channel is hydrophilic and composed mostly of Ser and Thr residues (31). PA_{bot} disrupted the lower *trans*-most portion of the β barrel and channel via the similar isosteric Thr substitutions (E302T, H304T, E308T, and H310T). The modeled electrostatic effects of these two mutant PA β barrels are shown in Fig. 5*A*.

The Ion Selectivity Filter of the PA Channel Is Critical for $\Delta\psi$*- and* ΔpH*-driven Translocation*—To characterize PA_{top} and PA_{bot}, however, we first needed to properly assemble the monomeric PA into oligomers. The multisite mutations would not assemble using the traditional ion-exchange approach (27). Hence we developed a modified assembly procedure. We nicked the PA monomers at pH 9 with furin instead of trypsin (to avoid nonspecific tryptic degradation), co-assembled the PA at pH 9 by adding LF_N (5, 23), and finally added Fos-choline-14 detergent to convert the prechannel oligomers into stable, detergent-solubilized channels (32). As a control, we also assembled WT PA by the same procedure. Native and SDS-PAGE (supplemental Fig. S2*A*) and negative-stain EM (supplemental Fig. S2*B*) verified the proper assembly of these samples. To monitor channel formation by planar bilayer electrophysiology, we had to remove the LF_N *in situ* by perfusing the *cis* chamber and translocating the residual LF_N through the chan-

nels. We found that Fos-choline-14 favorably weakened the interaction of LF_N with the channel, making its removal rapid and complete. In conclusion, the three preparations had reasonable insertion activities, albeit WT PA was most optimal.

To determine whether these mutations change the ion selectivity of the PA channel, we first measured $\Delta\psi_{rev}$ for WT PA, PA_{top}, and PA_{bot}. ($\Delta\psi_{rev}$ is the voltage required to reduce the ionic current to zero under asymmetrical KCl gradients.) Each of these complexes was applied to planar bilayer membranes to form stable populations of channels following the removal of excess LF_N by perfusion and translocation. The removal of residual LF_N was judged to be complete by the stabilization of the current. Over a range of tested KCl gradients (in unbuffered saline, pH 5.8), WT PA and PA_{bot} possessed similar $\Delta\psi_{rev}$ values and, therefore, possessed similar ion selectivity (Fig. 5*B*). However, PA_{top} showed a reduced magnitude of $\Delta\psi_{rev}$ relative to WT PA (Fig. 5*B*). Thus PA_{top} disrupts a portion of the ion-selectivity filter of the channel, presumably by reducing its anionic charge character (Fig. 5*A*).

PA_{top} and PA_{bot} were then assayed for their ability to translocate LF_N under either a $\Delta\psi$ or a ΔpH. We found strong translocation deficiencies for PA_{top} with either type of driving force (Fig. 5*C*). Under a 1-unit ΔpH (pH_{cis} 5.6 to pH_{trans} 6.6) with $\Delta\psi$ of 20 mV, translocation of LF_N through PA_{top} is slowed more than 10-fold compared with WT PA, whereas PA_{bot} is unaffected (Fig. 5*C, left*). With a 50 mV $\Delta\psi$ at symmetrical pH 5.6, PA_{top} was also less able to translocate LF_N relative to WT PA (Fig. 5*C, right*). Under these conditions, the rate and efficiency of translocation were affected. Although WT PA and PA_{bot} are fully translocated within 2 min, PA_{top} achieved less than 20% efficiency after 10 min. Thus PA_{top} reveals significant translocation deficiencies under either a $\Delta\psi$ or ΔpH driving force.

Finally, LF_N was assayed for its ability to block PA_{top} and PA_{bot} channels. In this experiment, we added 5 nM LF_N to the channels bathed in an asymmetrical KCl gradient at symmetrical pH 6.6 and a $\Delta\psi$ of 0 mV. Under these conditions, we found 99.0% (±0.1) of WT PA channel current was blocked (Fig. 5*D*). For PA_{bot}, we observed 98.0% (±0.1) conductance blockade; however, for PA_{top}, 88% (±1) of the conductance was blocked by LF_N. The binding defect observed with PA_{top} may indicate that the charge disruption in that region affects the ability of the amino terminus of LF_N to properly dock inside the pore and block conductance. In this model (Equation 3), we expect two different stages of binding. In stage one, LF_N binds to the top surface of the channel, forming the ($PA{\cdot}LF_N$) complex; and in stage 2, the amino terminus docks into the channel to block conductance, forming the ($PA{\cdot}LF_N$)* complex.

$$PA + LF_N \leftrightarrow (PA{\cdot}LF_N) \leftrightarrow (PA{\cdot}LF_N)^* \qquad \text{(Eq. 3)}$$

To test whether stage 1 or stage 2 were affected by the PA_{top} mutation, we determined the percent blockade as a function of LF_N concentration. Although the concentration of LF_N should affect the equilibrium of stage 1, the equilibrium describing stage 2 is, of course, concentration-independent. To test for these two possibilities, we altered the LF_N concentration. Reducing the concentration to 1 nM resulted in small changes in channel blockade (PA WT, 98.4% (±0.1); PA_{bot}, 97.0% (±0.3); PA_{top}, 86% (±2)). However, increasing the concentration 5-fold to 25 nM did not appreciably change the blockade (PA WT, 99.3% (±0.0); PA_{bot}, 98.7% (±0.2); PA_{top}, 88% (±1)), indicating that the system is at saturating levels of LF_N. Indeed, even increasing the concentration to 1.2 μM did not appreciably affect the percent block (Fig. 5*D*). The inability of LF_N to fully saturate channel conductance blockade in the PA_{top} mutant over a 1000-fold concentration range demonstrates that channel docking (stage two) is impaired, and the PA_{top} mutation likely disrupts a latching or ratcheting feature within the PA channel.

DISCUSSION

General Substrate Charge Requirements—To address the molecular mechanism of PMF-driven translocation, we traced the source of the differences in the translocation kinetics between LF_N and EF_N. Previous translocation studies (5, 8) and our more controlled re-examination here show that EF_N translocates ~200-fold slower than LF_N under a $\Delta\psi$ alone and ~10-fold slower than LF_N under a combined $\Delta\psi$ and ΔpH (Fig. 2, *B* and *C*). This phenomenon occurs despite the fact that LF_N and EF_N have ~55% sequence similarity, adopt identical folds (24, 26), possess similar solution stabilities (Fig. 2*D*) (31), and bind to the same location on the PA channel (4, 37). Interestingly, whereas LF and EF initiate translocation starting from the amino termini of their homologous LF_N and EF_N domains, the amino-terminal initiation sequence of these domains is the most divergent sequence in the domain. We anticipated that this region of the sequence was responsible for the differences we observed in their translocation kinetics. Swapping the 40-residue amino terminus of EF_N with the homologous 50-residue amino terminus from LF_N allows the chimera to translocate as rapidly as LF_N. The inability of EF_N to utilize the PMF as well as LF_N is hence due to sequence differences in the amino-terminal presequence, and therefore, the charged presequence is critical to allowing the substrate to best capture the PMF to drive unfolding and translocation.

Within the presequence, we were then able to locate two sequence cassettes, or motifs, required for efficient translocation (Fig. 3*B*). When additional acidic residues are added within the 20s cassette of EF_N, its translocation becomes more LF_N-like. Previous studies by Brown *et al.* (9) have shown that under a ΔpH driving force, acidic residues are needed in the 20s cassette for efficient translocation, and whereas our studies here support prior observations, they also show that higher acidic residue content in the 20s cassette is favorable under a pure $\Delta\psi$. Hence the acidic residue-dependent mechanism we observe is independent of the nature of the driving force. This dependence, at first glance, is most unusual because it is opposite to the effect expected for a *cis*-positive $\Delta\psi$, and we will expand on this point in detail below. But from this unusual charge requirement, we expect that the electrostatics of the channel itself govern the overall mechanism. We also identified a 40s cassette in the presequence and found it prefers cationic residues. This preference in the 40s cassette is only observed under a pure $\Delta\psi$ driving force, and whereas the 40s cassette is a novel sequence feature, it was expected to exist because a productive $\Delta\psi$ driving force is *cis*-positive.

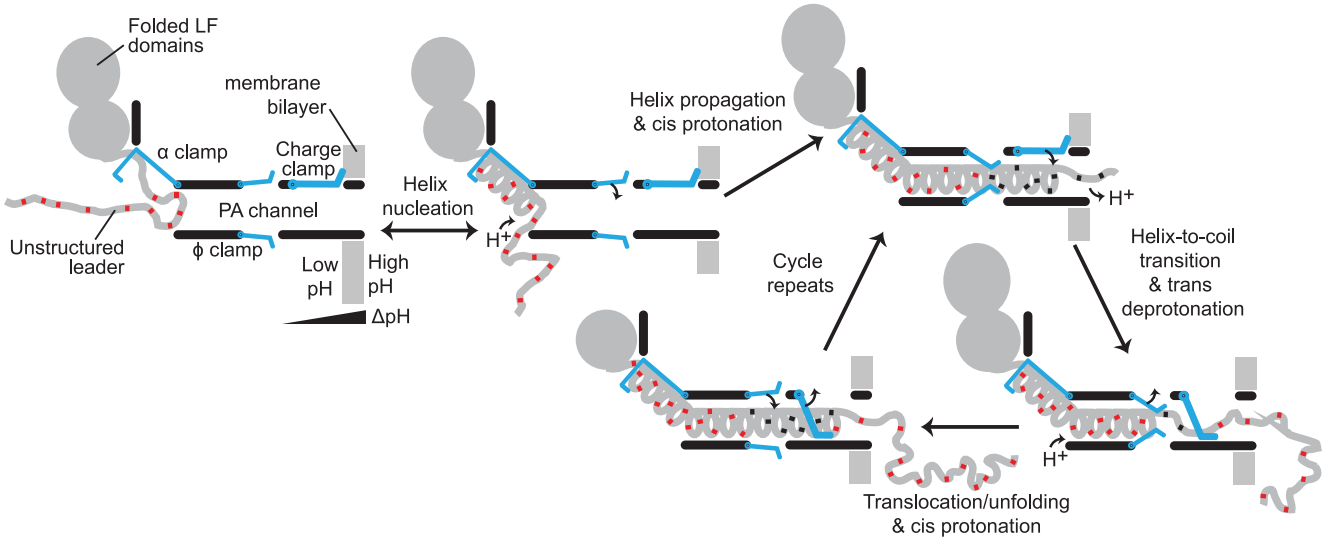

FIGURE 6. **Electrostatic ratchet model.** A schematic model of the PA channel (*black outline*) with the indicated α-, ϕ-, and charge-clamp sites (*blue moveable gates*) based on results described here and elsewhere (2, 4, 6–9). The folded substrate domains from LF are indicated as *gray circles* on the top surface of the channel, where its amino-terminal leader sequence is shown as a *thick gray line*. The α clamp may nucleate the helical structure into the channel, where the ϕ clamp can grip the amino-terminal leader. Protonation of the peptide on the lower pH side (*cis* protonation) converts acidic, charged residues (*red squares*) to neutral ones (*black squares*), allowing for the leader to move past the charge-clamp site via Brownian motion. Deprotonation of these acidic residues on the higher pH side (*trans* deprotonation) and an accompanying helix-to-coil transition in the leader are thermodynamically favorable and result in further translocation. The deprotonated sequence is, however, unable to retrotranslocate due to the charge-clamp site. Entropic tension in the upstream folded substrate maintained by the clamp sites leads to domain unfolding. Further cycles complete the translocation of the remaining domains.

Broad Sequence Specificity in Protein Translocases—The broad sequence specificity we observe for these charged cassettes (Fig. 4, *C* and *D*) is similar to the binding preferences of other polypeptide-clamping sites in the PA channel and in other systems (2). This observation is the case during translocation for several reasons. The sequence complexity is high, meaning the amino acid sequences, which continually pass through the channel, cover an enormous combinatorial sequence space. Also, the conformational and configuration space the translocating chain may explore during translocation is enormous. Levinthal (40) originally stated that a folding protein would be unable to sample all the possible configurations of the unfolded state in a reasonable time scale, and instead, proteins must fold via a specific pathway. The hydrophobic effect, for example, is likely a key feature that guides many folding pathways. Hence, we propose that broad sequence specificity is key for a protein translocase, because it must process unfolded protein, which may otherwise occupy too many possible states.

The charged cassettes we report here again have general electrostatic requirements, but the specific details are far less critical. Other examples of these nonspecific clamping sites in the PA channel include the α clamp and the ϕ clamp. The ϕ clamp prefers hydrophobic and aromatic substrates (7), whereas the α clamp binds most optimally to α-helical structure with minimal sequence specificity (4). Each clamping site binds broadly to a different type of chemical handle in the translocating chain, where specific hydrogen bonds and salt bridges are noncritical. Polypeptide clamps are critical because forces cannot be applied to the unfolding substrate protein without a fulcrum. Also, competing diffusive and entropic forces in the system scale with the size of the unfolded state; *i.e.* for an *n*-residue long unfolded chain where each residue can sample an average of *C* conformations, the total number of potential configurations scales as C^N. Limiting the size of the unfolded chain that is freely diffusible through nonspecific clamping allows the force-generating apparatus to focus more efficiently on producing directional motion and mechanically unfolding the substrate. The downside to nonspecifically clamping the chain becomes immediately apparent; because when interactions are too tight translocation should become impeded. However, we have proposed instead that clamping sites are dynamic, and the chain is continually bound and released during translocation, and hence such events would reduce diffusive entropic costs, improve energy transduction and force generation, and lower the overall barriers to translocation.

Role of Channel Electrostatics in Translocation—Previous work by Brown *et al.* (9) has shown that sites within the 20s cassette of LF_N were optimal for the placement of acidic residues when translocation is driven by a ΔpH. The key finding in this report is that EF_N chimeras also require additional acidic residue density in the 20s cassette; however, this requirement for more rapid translocation kinetics holds even under a pure Δψ driving force. The requirement is counterintuitive because the relationship expected between a purely Δψ-driven process and charge should rather be a preference for cationic residues. Because the acidic residue requirement in the 20s cassette is driving force independent, we surmised that the electric field acting on the negatively charged region is not purely derived from the Δψ (as that would create forces opposite in sign to productive translocation) but rather from charged residues residing inside the PA channel.

Simplified electrostatic modeling of the PA channel β barrel reveals two strong oppositely charged electrostatic barriers/wells are present depending upon the identity of the test charge used (Fig. 5*A*). We started with the β barrel because the structure is well supported by numerous studies (19, 28, 29). The

electrostatic features we identified in the β barrel are produced by residues pointing into the lumen of the barrel and residues on the outside of the barrel. We mutated various residues in the β barrel in clusters to investigate their role in the translocation mechanism. The contribution of these charged residue mutations are, of course, amplified by the 7- to 8-fold nature of the oligomer. Based on our electrostatic modeling, PA_{bot} (which removed 4 charges per monomer, 2 positive and 2 negative) will have very modest effects on the electrostatic energy landscape; however, PA_{top} (which removed 3 negative charges) is expected to diminish the anion-repulsive barrier (Fig. 5*A*). We hypothesized that this would shift the ion selectivity and confirmed this to be true by measuring a reduction in $\Delta\psi_{rev}$ for PA_{top} relative to WT PA and PA_{bot} (Fig. 5*B*). This result implies that this region is part of the ion-selectivity filter. It should also be stated that other reports have implicated the ϕ-clamp site as a key electrostatic filter central to ΔpH translocation, albeit it is unclear what charged residue comprises the ϕ-clamp filter itself (18). We report here that when the charge-selective filter is removed from the PA_{top} mutant, both substrate docking and translocation are defective (Fig. 5, *C* and *D*). The inability to properly dock LF_N argues that a clamping or latching feature in the channel is disrupted in the PA_{top} mutation, and we suspect this element in the top of the PA β barrel is a key piece of the electrostatic ratchet expected in our BR model.

Model—Our BR model (Fig. 6) suggests that ion selectivity plays an important role in PMF-driven translocation (6, 9). We expect that a polypeptide chain can pass through the anion-repulsive charge filter once it is partially protonated by the lower *cis* pH. As this chain moves through the charge filter, the chain may deprotonate in the higher *trans* pH and become net repulsive to the charge filter. Such changes in the protonation state may also occur in the channel itself, because the residues we have identified in the PA_{top} mutant are also acidic, and this change would only favor the proposed model. At this stage, the filter acts like a ratchet and holds the chain in a way that limits retrotranslocation. An entropic tension develops in the leading sequence and favors further substrate unfolding of the lagging folded domain (9). In our current model, based upon the recent discovery of the helix stabilizing cleft, the α clamp, we propose that the helical structure can be stabilized inside of the channel. The transition from helix $\rightarrow$ random coil is highly favorable entropically, and thus should tend to thermodynamically drive the translocation of the chain from inside the channel to outside the chain during the deprotonation phase. Some coordination with the ϕ clamp site is evident in prior studies, and hence dynamics at the ϕ clamp site may be required for coordinated peptide movement or protonation state changes in the system (6). Brownian motion likely underlies the transitions in this system, especially when particular electrostatic barriers are lowered upon protonation/depronation cycles. Such diffusive motion is critical to driving the overall helix-to-coil transition we have proposed. This process can repeat in subsequent sequences and domains until translocation is complete.

It is tantalizing to point out that there is also a cation-repulsive site downstream of the anion-repulsive site in the β barrel. This cation-repulsive site will be stabilizing, however, to the formation of deprotonated Glu and Asp residues, favoring their deprotonation effectively. Such an activity would reinforce our BR model. The energy landscape we have computed is consistent with the biphasic nature of the $\Delta G^{\ddagger}$ *versus* charge relationship observed in the 20s cassette (Fig. 4*C*). One barrier prefers negative charge and the other prefers positive charge in the region. Based on these electrostatic features, the channel may hold amino-terminal polycationic substrates, such as His_6 tags (41), at low driving forces in a peptide-clamped or conductance-blocked stage indefinitely without actually translocating the substrate until a higher *cis*-positive potential is applied (6, 7, 9, 38). Many phenomena involving the amino-terminal presequences of LF, EF, and other heterologous substrates likely derive their origins from their interactions with the highly charged β barrel.

Acknowledgments—We thank P. Grob for technical support, E. Nogales for use of the electron microscope, and members of the Krantz laboratory for helpful advice and criticism.

REFERENCES

1. Thoren, K. L., and Krantz, B. A. (2011) The unfolding story of anthrax toxin translocation. *Mol. Microbiol.* **80,** 588–595
2. Feld, G. K., Brown, M. J., and Krantz, B. A. (2012) Ratcheting up protein translocation with anthrax toxin. *Protein Sci.* **21,** 606–624
3. Wickner, W., and Schekman, R. (2005) Protein translocation across biological membranes. *Science* **310,** 1452–1456
4. Feld, G. K., Thoren, K. L., Kintzer, A. F., Sterling, H. J., Tang, I. I, Greenberg, S. G., Williams, E. R., and Krantz, B. A. (2010) Structural basis for the unfolding of anthrax lethal factor by protective antigen oligomers. *Nat. Struct. Mol. Biol.* **17,** 1383–1390
5. Kintzer, A. F., Thoren, K. L., Sterling, H. J., Dong, K. C., Feld, G. K., Tang, I. I., Zhang, T. T., Williams, E. R., Berger, J. M., and Krantz, B. A. (2009) The protective antigen component of anthrax toxin forms functional octameric complexes. *J. Mol. Biol.* **392,** 614–629
6. Krantz, B. A., Finkelstein, A., and Collier, R. J. (2006) Protein translocation through the anthrax toxin transmembrane pore is driven by a proton gradient. *J. Mol. Biol.* **355,** 968–979
7. Krantz, B. A., Melnyk, R. A., Zhang, S., Juris, S. J., Lacy, D. B., Wu, Z., Finkelstein, A., and Collier, R. J. (2005) A phenylalanine clamp catalyzes protein translocation through the anthrax toxin pore. *Science* **309,** 777–781
8. Thoren, K. L., Worden, E. J., Yassif, J. M., and Krantz, B. A. (2009) Lethal factor unfolding is the most force-dependent step of anthrax toxin translocation. *Proc. Natl. Acad. Sci. U.S.A.* **106,** 21555–21560
9. Brown, M. J., Thoren, K. L., and Krantz, B. A. (2011) Charge requirements for proton gradient-driven translocation of anthrax toxin. *J. Biol. Chem.* **286,** 23189–23199
10. Galán, J. E., and Wolf-Watz, H. (2006) Protein delivery into eukaryotic cells by type III secretion machines. *Nature* **444,** 567–573
11. Tsai, B., Ye, Y., and Rapoport, T. A. (2002) Retro-translocation of proteins from the endoplasmic reticulum into the cytosol. *Nat. Rev. Mol. Cell Biol.* **3,** 246–255
12. Ruiz, N., Kahne, D., and Silhavy, T. J. (2006) Advances in understanding bacterial outer-membrane biogenesis. *Nat. Rev. Microbiol.* **4,** 57–66
13. Egea, P. F., Stroud, R. M., and Walter, P. (2005) Targeting proteins to membranes. Structure of the signal recognition particle. *Curr. Opin. Struct. Biol.* **15,** 213–220
14. Collier, R. J. (2009) Membrane translocation by anthrax toxin. *Mol. Aspects Med.* **30,** 413–422
15. Zhang, S., Udho, E., Wu, Z., Collier, R. J., and Finkelstein, A. (2004) Protein translocation through anthrax toxin channels formed in planar lipid bilayers. *Biophys. J.* **87,** 3842–3849
16. Pentelute, B. L., Sharma, O., and Collier, R. J. (2011) Chemical dissection of protein translocation through the anthrax toxin pore. *Angew. Chem. Int.*

Ed. Engl. **50,** 2294–2296
17. Pentelute, B. L., Barker, A. P., Janowiak, B. E., Kent, S. B., and Collier, R. J. (2010) A semisynthesis platform for investigating structure-function relationships in the N-terminal domain of the anthrax Lethal Factor. *ACS Chem. Biol.* **5,** 359–364
18. Basilio, D., Juris, S. J., Collier, R. J., and Finkelstein, A. (2009) Evidence for a proton-protein symport mechanism in the anthrax toxin channel. *J. Gen. Physiol.* **133,** 307–314
19. Katayama, H., Janowiak, B. E., Brzozowski, M., Juryck, J., Falke, S., Gogol, E. P., Collier, R. J., and Fisher, M. T. (2008) GroEL as a molecular scaffold for structural analysis of the anthrax toxin pore. *Nat. Struct. Mol. Biol.* **15,** 754–760
20. Lacy, D. B., Wigelsworth, D. J., Melnyk, R. A., Harrison, S. C., and Collier, R. J. (2004) Structure of heptameric protective antigen bound to an anthrax toxin receptor. A role for receptor in pH-dependent pore formation. *Proc. Natl. Acad. Sci. U.S.A.* **101,** 13147–13151
21. Petosa, C., Collier, R. J., Klimpel, K. R., Leppla, S. H., and Liddington, R. C. (1997) Crystal structure of the anthrax toxin protective antigen. *Nature* **385,** 833–838
22. Kintzer, A. F., Sterling, H. J., Tang, I. I., Williams, E. R., and Krantz, B. A. (2010) Anthrax toxin receptor drives protective antigen oligomerization and stabilizes the heptameric and octameric oligomer by a similar mechanism. *PLoS ONE* **5,** e13888
23. Kintzer, A. F., Sterling, H. J., Tang, I. I., Abdul-Gader, A., Miles, A. J., Wallace, B. A., Williams, E. R., and Krantz, B. A. (2010) Role of the protective antigen octamer in the molecular mechanism of anthrax lethal toxin stabilization in plasma. *J. Mol. Biol.* **399,** 741–758
24. Pannifer, A. D., Wong, T. Y., Schwarzenbacher, R., Renatus, M., Petosa, C., Bienkowska, J., Lacy, D. B., Collier, R. J., Park, S., Leppla, S. H., Hanna, P., and Liddington, R. C. (2001) Crystal structure of the anthrax lethal factor. *Nature* **414,** 229–233
25. Drum, C. L., Yan, S. Z., Bard, J., Shen, Y. Q., Lu, D., Soelaiman, S., Grabarek, Z., Bohm, A., and Tang, W. J. (2002) Structural basis for the activation of anthrax adenylyl cyclase exotoxin by calmodulin. *Nature* **415,** 396–402
26. Shen, Y., Zhukovskaya, N. L., Guo, Q., Florián, J., and Tang, W. J. (2005) Calcium-independent calmodulin binding and two-metal-ion catalytic mechanism of anthrax edema factor. *EMBO J.* **24,** 929–941
27. Blaustein, R. O., Koehler, T. M., Collier, R. J., and Finkelstein, A. (1989) Anthrax toxin. Channel-forming activity of protective antigen in planar phospholipid bilayers. *Proc. Natl. Acad. Sci. U.S.A.* **86,** 2209–2213
28. Benson, E. L., Huynh, P. D., Finkelstein, A., and Collier, R. J. (1998) Identification of residues lining the anthrax protective antigen channel. *Biochemistry* **37,** 3941–3948
29. Nassi, S., Collier, R. J., and Finkelstein, A. (2002) PA_{63} channel of anthrax toxin: an extended β-barrel. *Biochemistry* **41,** 1445–1450
30. Song, L., Hobaugh, M. R., Shustak, C., Cheley, S., Bayley, H., and Gouaux, J. E. (1996) Structure of staphylococcal α-hemolysin, a heptameric transmembrane pore. *Science* **274,** 1859–1866
31. Krantz, B. A., Trivedi, A. D., Cunningham, K., Christensen, K. A., and Collier, R. J. (2004) Acid-induced unfolding of the amino-terminal domains of the lethal and edema factors of anthrax toxin. *J. Mol. Biol.* **344,** 739–756
32. Vernier, G., Wang, J., Jennings, L. D., Sun, J., Fischer, A., Song, L., and Collier, R. J. (2009) Solubilization and characterization of the anthrax toxin pore in detergent micelles. *Protein Sci.* **18,** 1882–1895
33. Mueller, P., Rudin, D. O., Tien, H. T., and Westcott, W. C. (1963) Methods for the formation of single bimolecular lipid membranes in aqueous solution. *J. Phys. Chem.* **67,** 534–535
34. Robinson, R. A., and Stokes, R. H. (2002) *Electrolyte Solutions*, 2nd Ed., Dover, Mineola, NY
35. Pettersen, E. F., Goddard, T. D., Huang, C. C., Couch, G. S., Greenblatt, D. M., Meng, E. C., and Ferrin, T. E. (2004) UCSF Chimera. A visualization system for exploratory research and analysis. *J. Comput. Chem.* **25,** 1605–1612
36. Emsley, P., and Cowtan, K. (2004) COOT. Model-building tools for molecular graphics. *Acta Crystallogr. D* **60,** 2126–2132
37. Lacy, D. B., Mourez, M., Fouassier, A., and Collier, R. J. (2002) Mapping the anthrax protective antigen binding site on the lethal and edema factors. *J. Biol. Chem.* **277,** 3006–3010
38. Zhang, S., Finkelstein, A., and Collier, R. J. (2004) Evidence that translocation of anthrax toxin's lethal factor is initiated by entry of its N terminus into the protective antigen channel. *Proc. Natl. Acad. Sci. U.S.A.* **101,** 16756–16761
39. Woodhull, A. M. (1973) Ionic blockage of sodium channels in nerve. *J. Gen. Physiol.* **61,** 687–708
40. Levinthal, C. (1968) Are there pathways for protein folding? *J. Chim. Phys.* **65,** 44–45
41. Blanke, S. R., Milne, J. C., Benson, E. L., and Collier, R. J. (1996) Fused polycationic peptide mediates delivery of diphtheria toxin A chain to the cytosol in the presence of anthrax protective antigen. *Proc. Natl. Acad. Sci. U.S.A.* **93,** 8437–8442
42. Feld, G. K., Kintzer, A. F., Tang, I. I., Thoren, K. L., and Krantz, B. A. (2012) Domain flexibility modulates the heterogeneous assembly mechanism of anthrax toxin protective antigen. *J. Mol. Biol.* **415,** 159–174
43. Katayama, H., Wang, J., Tama, F., Chollet, L., Gogol, E. P., Collier, R. J., and Fisher, M. T. (2010) Three-dimensional structure of the anthrax toxin pore inserted into lipid nanodiscs and lipid vesicles. *Proc. Natl. Acad. Sci. U.S.A.* **107,** 3453–3457